nature energy

Article

https://doi.org/10.1038/s41560-023-01252-5

A salt-philic, solvent-phobic interfacial coating design for lithium metal electrodes

Received: 4 August 2022

Accepted: 17 March 2023

Published online: 24 April 2023

Check for updates

Zhuojun Huang[1,2,5], Jian-Cheng Lai[2,5], Sheng-Lun Liao[2], Zhiao Yu[2,3], Yuelang Chen[2,3], Weilai Yu[2], Huaxin Gong[2], Xin Gao[1], Yufei Yang[1], Jian Qin[2], Yi Cui[1,4] ✉ & Zhenan Bao[2] ✉

A key challenge to enable Li metal batteries as next-generation energy storage devices is to stabilize the interface between the Li metal and the electrolyte. A promising strategy is to promote the formation of a salt-derived robust and stable solid electrolyte interphase (SEI). Here we report a salt-philic, solvent-phobic (SP^2) polymer coating for Li metal electrode that selectively transports salt over solvent and thus promotes salt-derived SEI formation. Unlike previously reported artificial SEIs, this SP^2 coating approach resulted in enhanced cycling performance in several types of solvent, such as ether, carbonate and fluorinated ether. Specifically, the SP^2 coating further enhanced the cycle life of a recently reported high-performance fluorinated ether electrolyte to give a ~400 cycle life (50 µm Li, 2.5 mAh cm^{-2} nickel manganese cobalt oxide and 80% capacity retention). Our coating design concept can be further fine tuned as promising electrolytes become available.

Batteries with Li metal negative electrodes show great potential as next-generation energy storage devices due to their high theoretical specific capacity[1]. However, lithium metal batteries (LMBs) suffer from quick capacity fading. One major reason is the unstable interface between the lithium metal and the electrolyte[2]. Specifically, the solid electrolyte interphase (SEI) formed from Li metal contacting the electrolyte is non-uniform and fragile. It cracks and further grows in a uncontrolled way repeatedly during lithium metal plating and stripping[3]. Its heterogeneity is amplified throughout battery cycling, resulting in depositing whisker-shaped lithium and capacity fading[4].

To improve the performance of the negative electrode, there are three parallel routes: electrolyte engineering[5–11], interfacial design[12] or a hybrid of both[13,14]. As an interfacial design approach, applying a polymer layer to the Li electrode helps to stabilize this interface and promote the long-term operation of LMBs[15]. Polymers are desirable for their tunable chemical composition[16]. This polymer layer is expected to have both physical and chemical interactions with the underlying Li metal.

It is known that a viscoelastic polymer layer provides mechanical suppression of the Li metal and maintains a uniform coverage of the electrode during cycling[17–20]. By introducing moieties that interact with Li^+ (refs. 21,22) or alter the Li^+ solvation environment[23,24], a polymer layer can modulate the transport of Li^+ at the interface. A polymer layer may also have a favourable interaction with the electrolyte to promote ion transport at the interface[25,26]. Chemically, this polymer layer can react with Li metal[14,27,28] and produce an interfacial layer. For example, polyvinylidene fluoride is used as a layer to react with Li, and the reaction product, LiF, can homogenize the Li^+ flux at the interface. Polymers can also composite with other inorganic materials to improve the electron conduction and nucleation process[16,29,30]. The general aim is to produce a robust SEI, which is necessary to promote stable operation of the Li electrode[31,32].

When Li metal is in direct contact with the electrolyte, it typically reacts with both the lithium salt and the solvent to form a SEI. Many recent electrolyte designs populate the concept of an anion-rich inner solvation sheath[33,34]. The resulting salt-derived SEIs are robust and promote stable long-term operation of the battery[26,31,35].

[1]Department of Materials Science and Engineering, Stanford University, Stanford, CA, USA. [2]Department of Chemical Engineering, Stanford University, Stanford, CA, USA. [3]Department of Chemistry, Stanford University, Stanford, CA, USA. [4]Stanford Institute for Materials and Energy Sciences, SLAC National Accelerator Laboratory, Menlo Park, CA, USA. [5]These authors contributed equally: Zhuojun Huang, Jian-Cheng Lai. ✉e-mail: yicui@stanford.edu; zbao@stanford.edu

https://doi.org/10.1038/s41560-023-01252-5

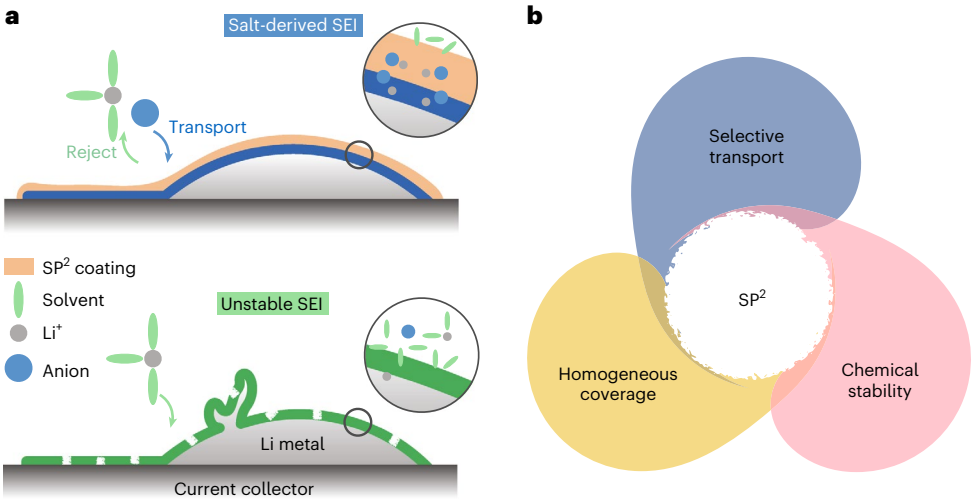

Fig. 1 | Design concept of the SP^2 coating. a, A polymer layer with selective salt-over-solvent transport capability can induce the formation of a robust salt-derived SEI (top), and an unstable SEI is formed when Li reacts with the electrolyte non-selectively (bottom). **b**, The material requirements of the SP^2 coating.

In this article, we propose a design concept of using a polymer coating to promote the salt-derived SEI formation. Our polymer design, based on a polysiloxane backbone, was found to be applicable to several typical electrolyte chemistries (ether, carbonate and fluorinated ether). In the full cell cycling, cells with polymer-coated 50-µm-thick Li negative electrodes and 2.5 mAh cm^{-2} lithium nickel manganese cobalt oxide (NMC)-positive electrodes experience a ~2.5-fold increase in cycle life (80% capacity retention) in the carbonate electrolyte, and a ~2-fold increase in the fluorinated ether electrolyte.

Materials design

We hypothesize that, if a polymer coating allows the selective transport of lithium salts instead of solvent molecules, salts would have a higher probability of being in physical contact with the Li metal. This can promote salt-derived SEI formation (Fig. 1a). Our strategy intercepts the self-amplifying process of heterogeneous Li deposition by tuning the chemical composition of the SEI. Our polymer design incorporates both salt-philic and solvent-phobic (SP^2) moieties as polymer side chains to facilitate the selective transport. The molecular design requirements for this coating are selective transport of salt over solvent, viscoelasticity to maintain electrode coverage and chemical stability (Fig. 1b).

Siloxane-based polymers have been shown to improve the coulombic efficiency (CE) in Li||Cu cells[36]. Beyond its chemical stability, the polysiloxane chain is flexible and has a low glass transition temperature (about −150 °C) (ref. 37). The fluid nature of the siloxane backbone offers flexibility in altering the chemical compositions of the polymer via side chain engineering, while maintaining the viscous mechanical property of the polymer[38]. Past theoretical and experimental studies have shown that a viscous artificial SEI prevents cracks and pinholes. It also helps to maintain an uniform Li^+ transport during cycling[19]. In this study, we selected four types of side chain to systematically investigate the effects of salt versus solvent reactivity on the cycling stability of Li: (1) glyme, a salt-solvating unit that is often used as an electrolyte solvent[39], (2) pyrrolidinium bis(trifluoromethylsulfonyl) imide (PyTFSI), an electrochemically stable salt-solvating ionic liquid moiety[40], (3) a perfluorinated side chain, which has poor solubility of the lithium salt and repels most other organic solvents[20,41] and (4) an alkyl chain, also not salt-solvating, but miscible with many non-polar organic solvents. Furthermore, a previous study demonstrated that polymer coating with a Py^+ cationic side chain improved Li deposition morphology. Specifically, Py^+ shielded Li^+ from charging surface protrusions during deposition via electrostatic repulsion[42]. Figure 2a shows the corresponding chemical structures.

We first examined the salt philicity by measuring the solubility of the LiTFSI salt in the small-molecule version of the corresponding polymer side chain. Specifically, we selected diglyme for the glyme side chain; hexane for the alkyl; 1,1,1,2,2,3,3,4,4-nonafluoro-6-propoxyhexane for the perfluorinated side chain; and Py_{14}TFSI for the ionic liquid (Supplementary Fig. 1). As seen from the saturated molar ratio of LiTFSI to these molecules (Fig. 2b), both the diglyme and Py_{14}TFSI dissolve a good amount of LiTFSI salt (molar ratios of 1.25 and 0.5, respectively)[39,43]. In comparison, hexane exhibited poor salt solubility, and no LiTFSI signal was detected in the ^{13}C nuclear magnetic resonance (NMR) spectrum. The 1,1,1,2,2,3,3,4,4-nonafluoro-6-propoxyhexane can solvate a small amount of LiTFSI (molar ratio 0.01, ^{19}F NMR; Supplementary Fig. 2), showing a low level of salt philicity. We cross-validated the trend of the salt philicity with a density function theory (DFT) simulation, where the interaction energy between the model side chain and the LiTFSI salt was calculated (Supplementary Fig. 3). We found the trend in salt philicity agreed with the trend in salt solvation: alkyl has the lowest interaction energy (71 kJ mol^{-1}), glyme has the highest interaction energy (234 kJ mol^{-1}) and PyTFSI has a relatively high interaction energy (189 kJ mol^{-1}) (Fig. 2b).

Beyond the salt philicity, we further characterized the solvent phobicity of various polymer side chains through contact angle measurements. A more solvent-philic polymer is expected to exhibit a lower contact angle with the corresponding solvent. To perform this study, we dropped 10 µl of the following solvents to polymer-coated silica wafers: (1) carbonate (ethylene carbonate, diethyl carbonate (EC/DEC), with 10% fluoroethylene carbonate (FEC)), (2) ether (1,3-dioxolane, dimethoxyethane (DOL/DME)) and (3) fluorinated ether (fluorinated 1,4-dimethoxylbutane (FDMB))[44]. These solvents were selected from commonly used electrolyte formulations[45]. In addition to having a high affinity to lithium salt, the glyme side chain was found to be solvent philic, as seen from the low (<8°) contact angles for all three solvent types. In comparison, the polymer with the salt-philic PyTFSI side chain has higher contact angles (~20° for ether and fluorinated ether, ~35° for carbonate). Both the alkyl and the perfluorinated side chains showed higher levels of solvent phobicity on the basis of their contact angles of 30–40° for (fluorinated) ether solvents and >50° for carbonate solvents (Fig. 2c). We also examined the solvent phobicity of these polymers in the presence of salts. Specifically, we measured the contact angles of electrolytes in the same experimental setup. Electrolytes used were ether (1 M LiTFSI DOL/DME 1 wt% $LiNO_3$), carbonate (1 M $LiPF_6$ EC/DEC 10% FEC, lithium hexafluorophosphate) and fluorinated ether (1 M LiFSI, FDMB, lithium bis(fluorosulphonyl)imide) (Supplementary

https://doi.org/10.1038/s41560-023-01252-5

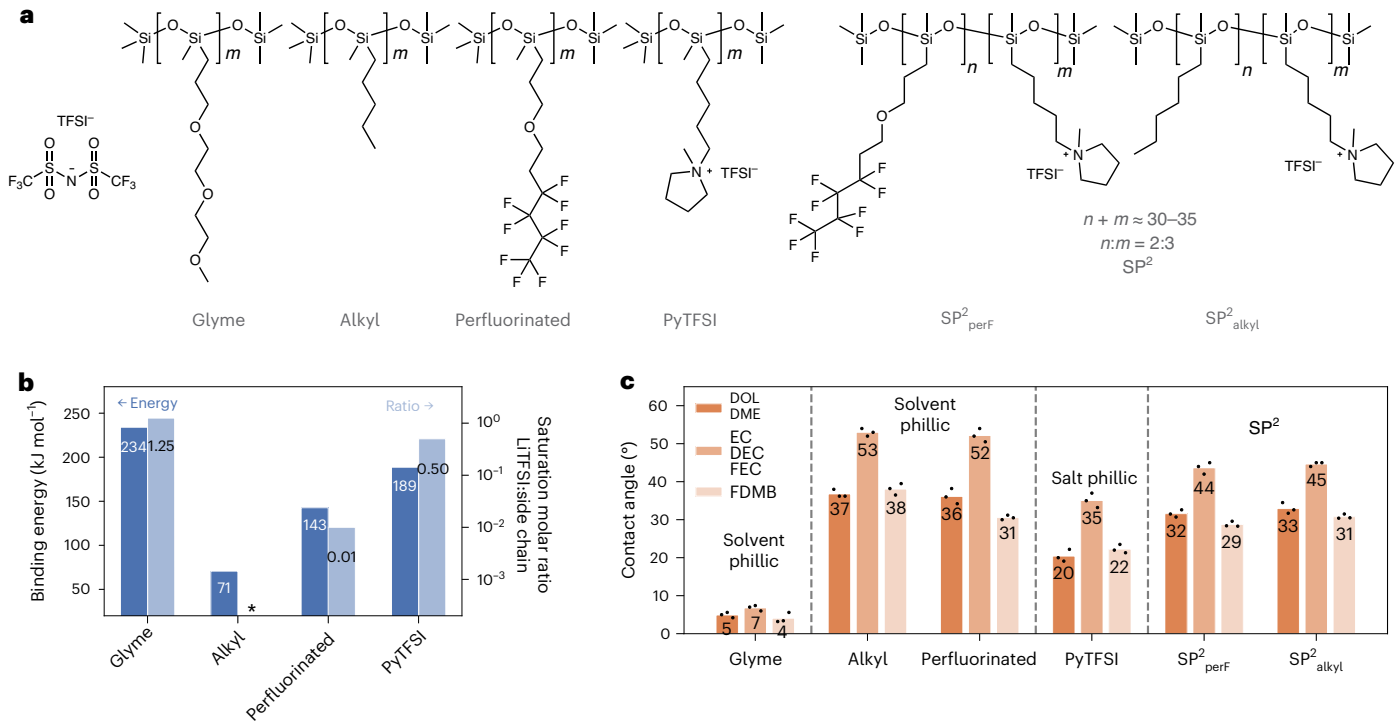

Fig. 2 | Characterization of the salt philicity and the solvent phobicity of polymers and side chains. a, The chemical structures of polymers with different side chains that represent various levels of salt philicity and solvent phobicity, and the strucutre of the TFSI anion. **b**, The salt philicity of the polymer side chains quantified by DFT and NMR: the interaction energy between Li salt and the side chain was calculated from DFT, and the saturation of Li salt concentration measured with NMR. *Not detected. **c**, The contact angle measurements on polymer-coated Si wafers with three types of solvent, including ether (DOL/DME), carbonate (EC/DEC/FEC) and FDMB.

Fig. 4). When salts were present, the contact angles of ether and fluorinated electrolytes were slightly higher (2–5°) than in the case with no salt (Supplementary Fig. 5). However, this did not change the overall observed correlation between the polymer chemistry and the solvent phobicity.

We identified the PyTFSI side chains as salt philic with a moderate solvent phobicity. To further increase the solvent phobicity of the polymer, we replaced 40% of the PyTFSI side chains with perfluorinated chains (SP^2_{perF}) or alkyl chains (SP^2_{alkyl}). SP^2_{perF} increased the contact angle from 20° to 32° in ether, from 35° to 44° in carbonate and from 22° to 29° in fluorinated ether solvents, and SP^2_{alkyl} showed similar improvements (Fig. 2c). This design strategy produces a polymer coating that is expected to selectively transport salt over solvent.

As a summary, we investigated six different polymers, each representing a different level of salt philicity and solvent phobicity: glyme is salt philic but not solvent phobic, alkyl and perfluorinated chains are solvent phobic but not salt philic and PyTFSI is salt philic and has moderate solvent phobicity; SP^2 designs have both salt-philic and solvent-phobic moieties.

Selective transport of salt over solvent

To characterize the selective transport of the SP^2 polymer, we designed an H-cell experiment using the polymer as the bridge (Fig. 3a). The left-hand side (LHS) of the H-cell was initially filled with 3 ml of 1 M LiTFSI DME electrolyte, and the right-hand side (RHS) was filled with 6 ml DME solvent. The two sides were separated by two layers of separators with 100 mg of polymer sandwiched between them. As the system equilibrates, the concentration difference drives the diffusion of salt from LHS to RHS, and vice versa for the solvent. To avoid vacuum build-up upon solvent flowing, the caps of the H-cell were loosened. Figure 3b shows cartoons and digital images of the H-cell results. Visually, the lowering of the liquid line on the RHS is an indication of DME diffusion from right to left. The salt concentration was evaluated with ^{19}F NMR spectroscopy by comparing with a standard electrolyte (Supplementary Fig. 6). Exemplary spectra of the samples are shown in Supplementary Fig. 7, and the molarity calculation is summarized in Supplementary Table 1. To probe the detection limit of this NMR-based technique, we measured three dilute samples of the same concentration. We calculated the concentration of the solution as 8.4×10^{-3} M with a s.d. of 6.5×10^{-5} M (Supplementary Fig. 8 and Supplementary Table 2). With an error margin in the range of 10^{-5}, this NMR-based technique is sufficient to measure the salt concentration in this study, which is in the range of 10^{0}–10^{-2} M.

When there was no polymer present, the liquid levels of the two sides equilibrated after 3 h, indicating DME diffusion from right to left. There is also salt transport from LHS to RHS, resulting in the RHS salt concentration reaching 0.019 M. The polymer with PyTFSI side chains has medium solvent phobicity. When using PyTFSI polymer as the bridge, the liquid level on the RHS almost matched that of the LHS, indicating solvent migration. Since PyTFSI is salt philic, we observed enhanced LiTFSI transport compared with the no polymer scenario, with the RHS concentration reaching 0.051 M. When the SP^2_{perF} polymer was inserted, the liquid level difference was maintained for more than 3 h and the LHS salt concentration rose from 0 to 0.025 M, demonstrating selective transport of salt over solvent. We noted that the LiTFSI concentration remained at 1 M on the LHS instead of lowering, and we attributed this to the slight evaporation of DME. SP^2_{perF} polymer also showed selective transport at a higher salt concentration (starting condition: LHS, 3 ml 4 M LiTFSI DME; RHS, 6 ml DME). No appreciable solvent diffusion across the polymer was observed, while the LHS reached a concentration of 0.07 M after 3 h (Supplementary Fig. 9). Polymers with either perfluorinated or alkyl

https://doi.org/10.1038/s41560-023-01252-5

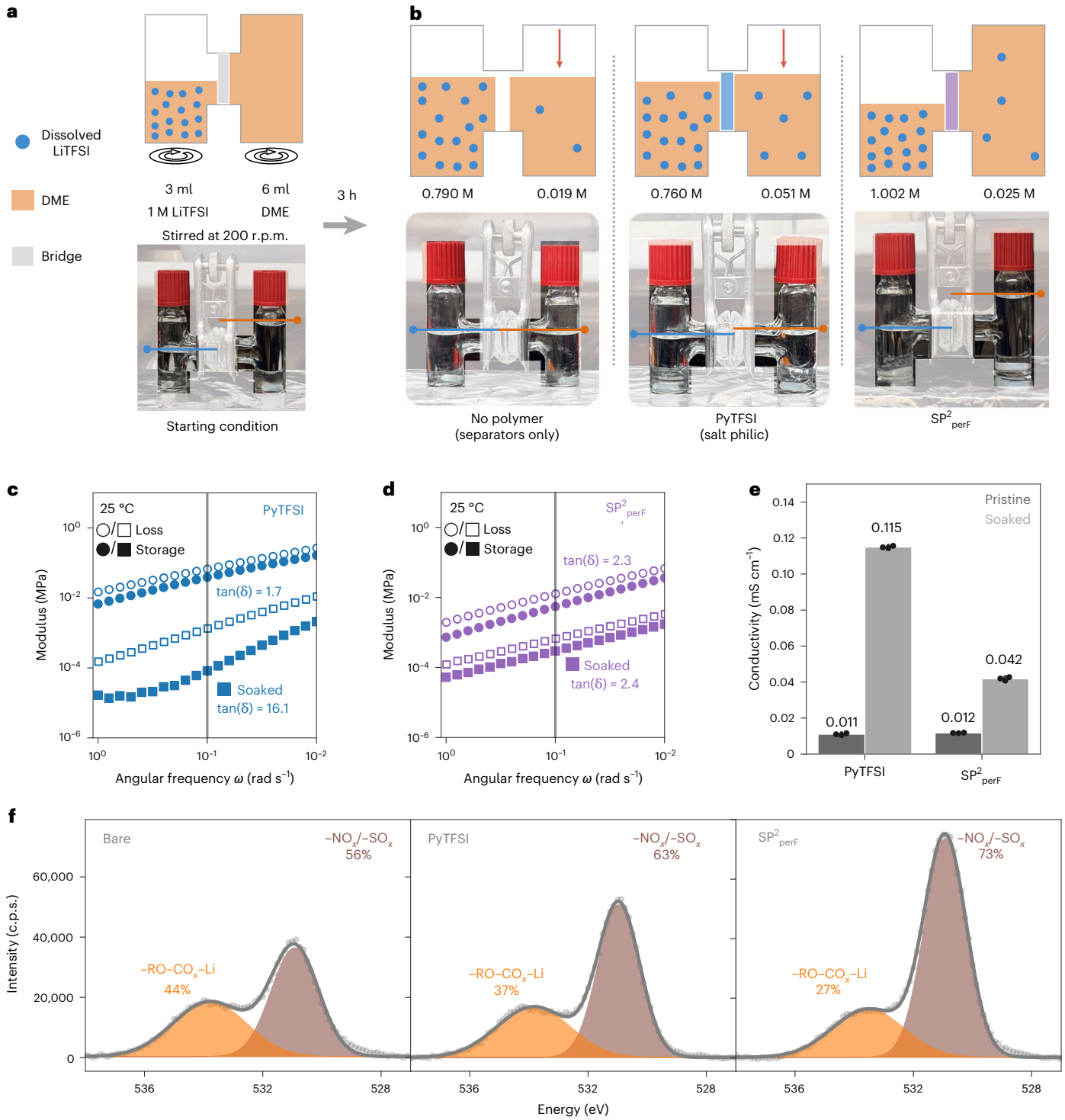

Fig. 3 | Selectivity of PyTFSI and SP^2_{perF} polymers. a, A cartoon (top) and digital image (bottom) of the H-cell experiment setup: 3 ml of 1 M LiTFSI on the LHS and 6 ml DME on the RHS. Circles with arrows represent stiring during the experiment and dot-capped lines in the digital image represent the liquid level. **b**, Cartoons (top) and digital images (bottom) of the H-cell experimental result. The blue dots roughly represent the LiTFSI concentration, the red arrows show the lowering of the liquid level and coloured blocks represent polymer bridges (blue: PyTFSI; purple: SP^2_{perF}). NMR-measured salt concentrations after 3 h are listed below the cartoons. **c**, **d**, Rheological frequency sweep of polymers PyTFSI (**c**) and SP^2_{perF} (**d**). A line is drawn at 10 rad s^{-1}, and the calculated tan(δ) (G''/G') at this frequency is listed. **e**, Conductivity (25 °C) of the polymer before and after soaking in DME solvent for 8 h. Individual measurements are represented by black dots, and the average of the three measurements is given. **f**, Oxygen O 1s XPS of SEI on the negative electrode, and the signals attributed to either salt or solvent decomposition are separated, with their relative percentage marked.

side chains were found to be solvent phobic (Fig. 2b), although the perfluorinated chain showed a slightly higher salt philicity (Fig. 2c). We sandwiched the SP^2_{alkyl} polymer in the H-cell with a starting condition of 1 M LiTFSI (as above; Supplementary Fig. 10). As with SP^2_{perF}, we observed the selective transport of salt over solvent. However, the concentration of LiTFSI on the LHS after 3 h was 0.01 M, lower than that of the SP^2_{perF}. We attributed this to the lower salt philicity of SP^2_{alkyl}.

https://doi.org/10.1038/s41560-023-01252-5

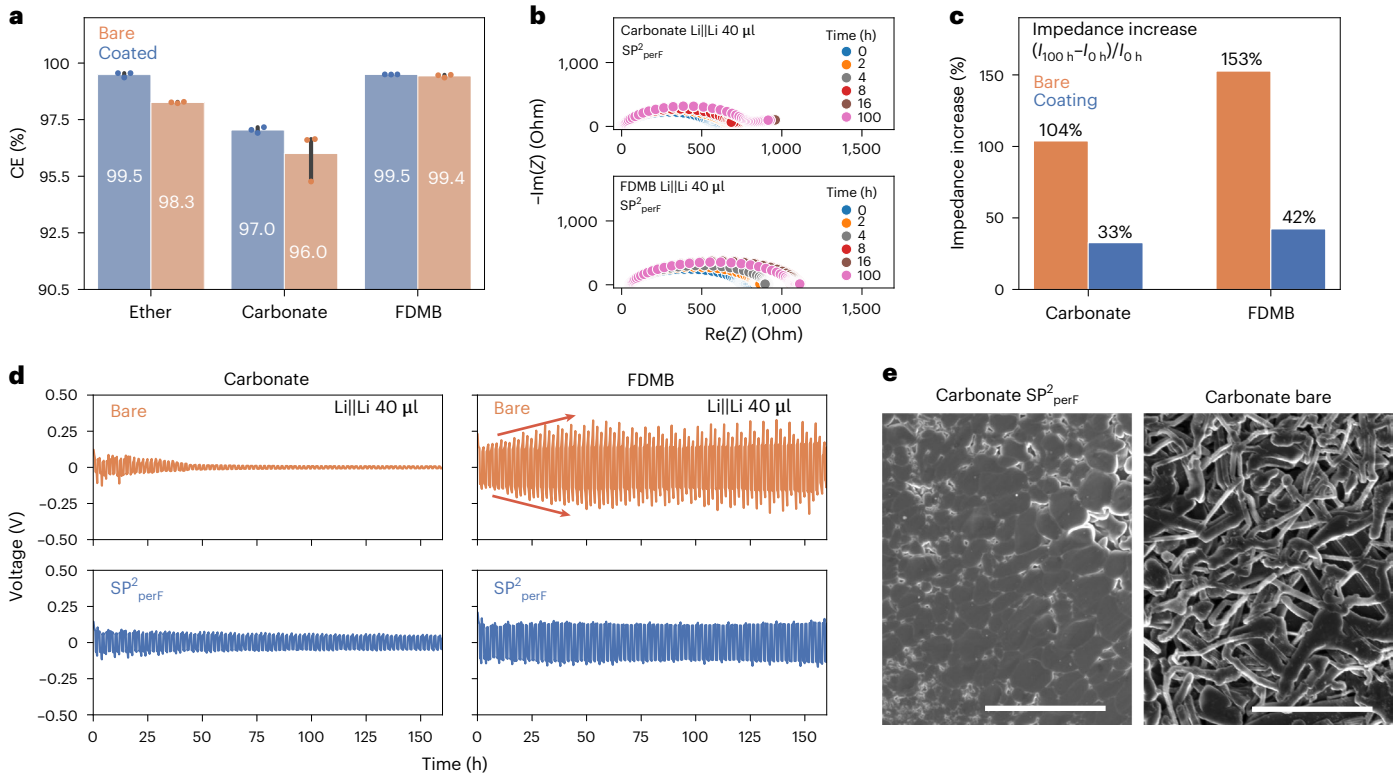

Fig. 4 | Electrochemical characterization of SP^2_{perF} with different electrolytes. **a**, The CE measured on coated Cu in Li||Cu cells with 40 µl of ether (1 M LiTFSI DOL/DME 1wt% $LiNO_3$), carbonate (1 M $LiPF_6$ EC/DEC 10% FEC) or FDMB (1 M LiFSI FDMB) electrolyte. Individual measurements, s.d. and averages of three measurements are represented by dots, black lines and listed numbers, respectively. **b**, EIS measurement over time with coated Li||Li symmetric cell in electrolytes. **c**, The calculated impedance increase (%) over 100 h. **d**, A voltage curve of Li||Li symmetric cell with and without SP^2_{perF} coating. **e**, SEM top view image of deposited Li on Cu electrode in carbonate electrolyte. Scale bar, 10 µm.

The integrated SP^2 design is applicable to other polymer chemistries. Specifically, we examined a previously reported acrylate-based polymer with ionic liquid and fluorinated alkyl side chains (PIL 15) (ref. 42). This coating also increased the salt-derived SEI content. In the H-cell experiment, PIL 15 demonstrated a salt-over-solvent transport behaviour (Supplementary Fig. 11). However, the PIL 15 polymer incorporated relatively few reactive functionalities such as urea bonds, limiting its ability to further improve the cycling performance.

The presence of a solvent-phobic side chain is also expected to limit the swelling of the polymer in solvents. Specifically, we compared the mechanical properties and ionic conductivities of the PyTFSI (Fig. 3c) and the SP^2_{perF} (Fig. 3d) polymers before and after soaking in DME. We characterized the frequency-dependent modulus of the polymer in the rheological measurement: the loss modulus (G'') represents the liquid characteristic and the storage modulus (G') represents the solid characteristic. We applied an oscillatory strain to the material and recorded its stress response. The G'' and G' values were acquired by separating the out-of-phase and in-phase responses. Before soaking, both the SP^2_{perF} and the PyTFSI polymers showed viscous behaviour, with G'' higher than G' in the characterized frequency range. After swelling, the polymer showed a decrease in both storage and loss moduli, indicating reduction in mechanical strength. Specifically, we characterized the relative liquid to solid characteristic of the polymer by calculating the tan(δ) (the ratio between G″ and G′) at the angular frequency of 10 rad s^{-1}. For the PyTFSI polymer, the tan(δ) increased by close to an order of magnitude (1.7 to 16) upon soaking, while the tan(δ) of the SP^2_{perF} polymer remained relatively constant (2.3 to 2.4). After swelling, the PyTFSI polymer becomes more liquid like, indicating that it is less resistive to solvent swelling. We also measured the ionic conductivities of the polymers before and after soaking (Fig. 3e) with electrochemical impedance spectroscopy (EIS) at 25 °C. The ionic conductivity is attributed to ionic dissociation of the PyTFSI. After soaking the polymer in the electrolyte, the conductivity of the PyTFSI polymer increased by an order of magnitude (0.011 to 0.115 mS cm^{-1}), while the conductivity of the SP^2_{perF} did not increase as much (0.013 to 0.042 mS cm^{-1}). This is consistent with the higher solvent resistance of the SP^2_{perF} polymer. On the basis of both the mechanical characterization and the ionic conductivity measurements, we concluded that the addition of the solvent-phobic side chain can reduce the solvent uptake.

We further examined the SP^2_{perF} polymer's ability to affect the SEI formation process. We assembled a Li||Cu cell with a polymer-coated Cu current collector. We stripped and plated Li through the polymer layer in 1 M LiTFSI DOL/DME 1 wt% $LiNO_3$ electrolyte for ten cycles to produce a layer of SEI underneath the polymer coating. Supplementary Fig. 12 shows the cross-section scanning electron microscopy (SEM) images of the SEI. The SEI on uncoated Cu is ~17.80 µm, with irregular granular structures. The SEI on SP^2_{perF} coated Cu was thinner (~12.86 µm) and initially covered with the polymer. We removed the polymer with tetrahydrofuran (THF), revealing the uniform and compact SEI underneath. The SEI chemistry was characterized with X-ray photoelectron spectroscopy (XPS). The XPS samples were not washed with solvents to preserve the original SEI chemistry. The O 1s spectra of the cycled Cu electrode after 2 min of sputtering are shown in Fig. 3f. When the Cu surface was not sputtered, we observed a large amount of C and Si signals. After 1 min of sputtering, the C signal reduced and the Si signal was no longer recognizable, which indicated that the polymer layer was removed. Further sputtering did not change the observed spectrum, indicating that the SEI composition was not influenced by the sputtering process (Supplementary Fig. 13). We attributed the peak at 530.9 eV to $-NO_x/SO_x$ (salt breakdown) and the peak at 533.8 eV

https://doi.org/10.1038/s41560-023-01252-5

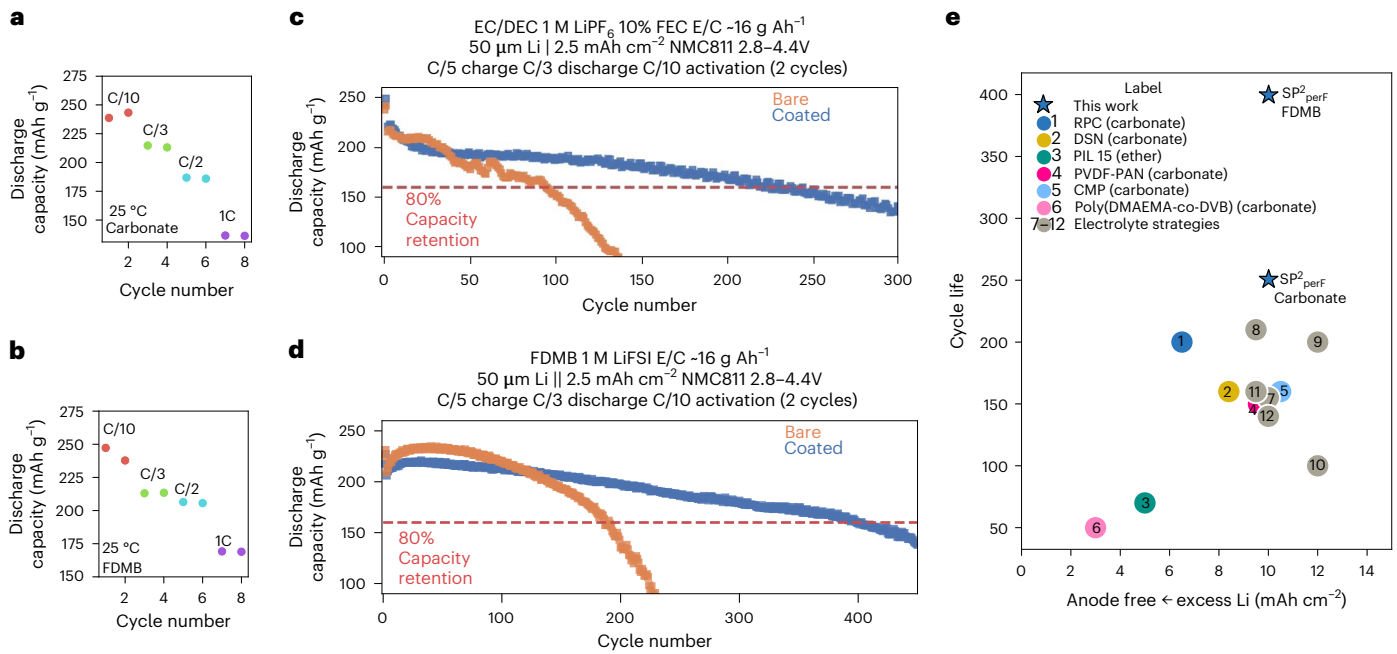

Fig. 5 | Cycling of SP^2$_{perF}$ coated Li in Li | |NMC cells. a,**b**, Rate capabilities with carbonate (**a**) and FDMB (**b**) electrolytes. **c**,**d**, Long-term cycling with carbonate (**c**) and FDMB (**d**) electrolytes. **e**, A comparison of cycle life (80% capacity retention) plotted against excess lithium amount of the SP^2$_{perF}$ coating with other coatings/electrolyte strategies. The *x*-axis locations of 4, 5, 7, 11 and 12 are 10 mAh cm^{-2}, and they are adjusted slightly to dodge.

to –RO–CO$_x$–Li (solvent breakdown). By calculating the percentage of the peak area attributed to salt/solvent breakdown, we can quantify the ability of the polymer to induce salt-derived SEI formation. When there was no coating, 56% of the SEI was attributed to salt decomposition. When the PyTFSI polymers were present, the salt-derived SEI content increased to 63%. This content can be further improved to 73% when the SP^2$_{perF}$ coating was present. We also found SP^2$_{perF}$-coated samples had higher salt-derived content at different rinsing (improved from 14% to 31%) and sputtering conditions (Supplementary Fig. 14). We further examined the SEI chemistry when SP^2$_{perF}$ was paired with the carbonate (1 M LiPF$_6$ EC/DEC with 10% FEC), as well as the fluorinated ether (1 M LiFSI in FDMB)[44] electrolyte through calculating the elemental ratio. For XPS measurements, the carbon signal was derived from solvent breakdown, while P, S and F signals were derived only from salt breakdown. A higher ratio of P, S or F to C reflects a more salt-derived SEI. Compared with the bare sample, SP^2$_{perF}$ increased the P/C intensity ratio from 2.94×10^{-2} to 1.48×10^{-1} in the carbonate electrolyte and increased the S/C intensity ratio from 9.62×10^{-2} to 2.55×10^{-1} in the FDMB electrolyte. In additive-free ether (1 M LiTFSI DOL/DME) or carbonate (1 M LiPF$_6$ EC/DEC) electrolytes, SP^2$_{perF}$ increased the S/C (ether) and F/C (carbonate) ratios by approximately threefold, and consistent results were observed at different sputtering times (Supplementary Fig. 15). Due to the selective transporting ability of the SP^2$_{perF}$ polymer, the deposited Li has limited access to solvent molecules, and a more salt-derived SEI is formed at various electrolyte conditions[34].

Electrochemical cycling

We investigated the coating's stability on the electrode at both the macroscopic and the microscopic scale. During in situ optical cell cycling, SP^2$_{perF}$ maintained coverage of the electrode surface, resulting in a homogeneous Li deposition underneath the coating. In contrast, on bare electrodes, Li deposits irregularly at locations of high electric field concentrations (Supplementary Fig. 16). We also took cross-section SEM images of Li cycled at 0.2 mA cm^{-2} and 0.5 mA cm^{-2} current densities and observed our coating remaining on the Li surface (Supplementary Fig. 17). After rinsing off the polymer coating, we revealed relatively homogeneous Li deposition. We compared the viscosities of the electrolyte-swelled polymer and just the electrolyte. The viscosity of the soaked polymer complex is four to five orders of magnitude higher (Supplementary Fig. 18).

The ability of the SP^2$_{perF}$ polymer to tune the SEI's composition led to marked improvements in the cycling performance in Li||Cu cells. As shown in Fig. 4a, we compared the CE under a short-term ten-cycle 0.5 mA cm^{-1} 1 mAh cm^{-1} cycling protocol[46]. In 1 M LiTFSI DOL/DME 1 wt% LiNO$_3$ electrolyte, the coating increased the CE from 98.3% to 99.5%. In the carbonate electrolyte, the CE increased from 96.0% to 97.0%. In the FDMB electrolyte, since the baseline electrolytes already achieves a high CE in this short-term cycling protocol, we observed a small increase with the addition of a SP^2$_{perF}$ coating (from 99.4% to 99.5%). We also cycled Li||Cu cells, and found SP^2$_{perF}$ can also increase the CE in standard carbonate and ether electrolytes (Supplementary Fig. 19). The improvement in CE with a layer of coating is higher for electrolytes without additives. This is because the more advanced electrolyte has limited room for improvement. We also paired the SP^2 coating with the state-of-the-art Li metal electrolyte: 1.2 M LiFSI in 1,2-bis(2,2-difluoroethoxy)ethane (F4DEE)[33], and the CE increased from 99.5% to 99.6% (Supplementary Fig. 20).

The SP^2$_{alkyl}$ polymer has a lower salt philicity compared with SP^2$_{perF}$, but still shows selective transport of salt over solvent. To examine the performance of an SP^2$_{alkyl}$ battery, we cycled SP^2$_{alkyl}$-coated Li||Cu cells with the previously mentioned short-term cycling protocol. For the carbonate electrolyte, SP^2$_{alkyl}$ improved the performance (CE increased from 96.0% to 96.6%). However, in the FDMB electrolyte, the CE decreased from 99.4% to 98.9%. Supplementary Fig. 21 shows the average and s.d. of deposition overpotentials (absolute values) for Li||Cu cells. The SP^2$_{alkyl}$-coated cell has a higher overpotential (0.049 V) than the SP^2-coated cell (0.041 V), and the s.d. was doubled. Due to the lower salt philicity of SP^2$_{alkyl}$, the ion transport at the electrode interface was impeded. Especially in electrolytes with limited ionic conductivity, the large deposition overpotential drives undesirable degradation (low CE) and operational instability (high s.d.)[33,47]. Overall, we found that it is critical to fine tune the balance between the solvent

phobicity and salt philicity, and the SP^2_{perF} coating showed a superior cycling performance.

Since both the carbonate and the FDMB electrolytes were cycled with the Li||NMC configuration, we characterized how SP^2_{perF} coating affects the electrolytes' stability with Li through EIS measurements and long-term cyclings of Li||Li cells. Figure 4b shows the interfacial impedance of SP^2_{perF}-coated Li in carbonate or FDMB electrolytes at different timepoints. The uncoated cells were used as comparison. For both electrolytes, the SP^2_{perF} layer was observed to suppress the impedance increase. We measured the impedance value at no rest and 100 h of rest (Supplementary Fig. 22). We quantified the increase with the formula $(I_{100} - I_0)/I_0$ (%). For the first 100 h, SP^2_{perF} reduced the impedance increase from 104% to 33% in the carbonate electrolyte and from 153% to 42% in the FDMB electrolyte (Fig. 4c). Since the polymer was coated on the Li surface with the THF solvent, we also examined THF's influence on the interfacial impedance. We treated bare Li metal with THF and tracked its impedance evolution in the carbonate electrolyte (Supplementary Fig. 23). With or without THF treatment, Li electrodes experienced a similar ~100% impedance increase, indicating that the SP^2_{perF} polymer is the reason for the reduced impedance increase.

We also cycled Li||Li symmetric cells at 1 mA cm^{-2} current density and 1 mAh cm^{-2} capacity (Fig. 4d). For the carbonate electrolyte, the addition of SP^2_{perF} coating resulted in a higher deposition overpotential, which was stable over cycles. For the uncoated Li electrode, the overpotential decreased between 25 and 40 cycles. This is due to an increase in the surface area from the irregular whisker-shaped lithium deposition[48], which was verified by SEM (Fig. 4e). The addition of the SP^2_{perF} coating promoted homogeneous deposition. For the FDMB electrolyte, a layer of SP^2_{perF} polymer maintained a stable overpotential over time. Without the SP^2_{perF} coating, the FDMB electrolyte continued to react with the lithium metal and increased the deposition overpotential[44]. In both cases, a layer of SP^2_{perF} coating limited the solvent breakdown at the Li electrode and sustained a stable operation.

To further understand the range of solvent phobicity and salt philicity required at the interface, we assembled Li||Cu cells with a solvent-philic polymer coating (siloxane-glyme). In the carbonate electrolyte, this coating had a limited improvement on CE (96.0% to 96.1%, Supplementary Fig. 24). The lithium deposition morphology remained whisker shaped (Supplementary Fig. 25). This confirmed the importance of a solvent-phobic interface.

SP^2_{perF}-coated thin Li negative electrodes (50 µm) were also assembled into Li||NMC cells. To understand how the SP^2_{perF} coating performs when there is initial Li presence, we built asymmetric cells of thin coated Li||thick Li (50 µm||600 µm). The uncoated cell experienced an overpotential increase at around 70 h while the coated cell had stable overpotential (Supplementary Fig. 26). SEI and dead Li formation on the thin Li reduces the ion and electron conductivity at the interface, contributing to the increased overpotential. This experiment allowed us to isolate the performance of just the SP^2_{perF}-coated Li electrodes. We also cycled Li||NMC full cells at different C rates (2.5 mAh cm^{-2} areal capacity) and found reasonable capacity (>200 mAh g^{-1}) can be achieved at C/10 and C/3 for both the carbonate and the FDMB electrolytes (Fig. 5a,b). For the high-capacity cathodes (5 mAh cm^{-2}), reasonable capacity was achieved at C/10 and C/5 C rates (Supplementary Fig. 27). We proceeded with C/5 charging and C/3 discharging for the long-term cycling. We cycled full cells with 2.5 mAh cm^{-2} NMC-positive electrodes. For the carbonate electrolyte, a cycle life of ~240 was reached (Fig. 5c) and for FDMB electrolyte, a cycle life of ~400 was reached (Fig. 5d). The CE of each cycle for both carbonate and FDMB electrolytes is shown in Supplementary Figs. 28 and 29. The charging voltage profile of the 100th cycle for the FDMB electrolyte is shown in Supplementary Fig. 30, with the coated sample showing a higher overpotential. Other repetitions of the cell are shown in Supplementary Figs. 31 and 32, where a similar trend of SP^2_{perF} coating increasing the cell cycle life was observed. We tested the Li||NMC cell with a higher-capacity (5 mAh cm^{-2}) positive electrode in the FDMB electrolyte, and found an increase (close to twofold) in the cell cycle life (Supplementary Fig. 33). We further tested the Li||NMC cell at the lean electrolyte condition (~3 g Ah^{-1}) and SP^2_{perF} improved the performance two- to fourfold in the carbonate electrolyte (Supplementary Fig. 34). Our SP^2_{perF} polymer design is applicable to various electrolyte chemistries and configurations, and is a marked improvement in cell cycle life versus excess Li amount when compared with other state-of-the-art strategies (Fig. 5e and Supplementary Table 3)[7,14,21,24,42,49–55].

Conclusions

The chemistry of the SEI is crucial for the stable operation of LMBs. In this work, we demonstrated a SP^2 interfacial design that promoted the formation of the salt-derived SEI and improved the cycling performance. Through physical interactions, we tuned the chemical reaction at the electrode–electrolyte interface. We optimized our coating through material and electrochemical characterizations, and we arrived at a polymer composition that can improve the cell performance in three major electrolyte categories (ether, carbonate and fluorinated ether). In full cell cycling, our coating improved the battery cycling performance with a state-of-the-art electrolyte. The SP^2 design concept can be extended to other polymer chemistries and potentially pair with other emerging electrolytes.

Methods

Materials

LiTFSI was purchased from Tokyo Chemical Industry; LiFSI from Fluolyte; polymethylhydrosiloxane, trimethylsilyl terminated (siloxane polymer backbone, molecular weight of 2,100–2,400 g mol^{-1}) and glyme side chain from Gelest and 1 M $LiPF_6$ in EC/DEC electrolyte from Gotion. Other general chemicals used in this study were purchased from Sigma-Aldrich. For a detailed polymer synthesis method[56], please refer to Supplementary Notes and Supplementary Figs. 35–50. The NMC-positive electrode was purchased from Targray. Thin lithium foil (50 µm) was purchased from Uniglobe Kisco Inc. The Celgard 2325 separator was purchased from Celgard. Cu electrodes, lithium chips (600 µm), 2032-type battery casings, stainless steel spacers, springs and Al-clad coin cell cases were purchased from MTI Corporation.

DFT calculations

The geometry optimizations and the energy for the ground states were calculated by DFT at the M06-2X/6–311G ++ (d, p) level . All DFT calculations were carried out with Gaussian 16 on Sherlock server at Stanford University.

Materials characterization

To apply a layer of polymer coating on Cu or Silicon wafer, 100 mg of polymer was dissolved in 1 ml of acetonitrile or 1,3-trifluorobenzene. The polymer was spin coated on the substrate at 1,000 r.p.m. spin rate. The coated sample was dried in a vacuum oven at 80 °C for 24 h to further remove organic solvents[42]. The coating thickness was characterized by a profilometer to be around 0.2 µm. The contact angle was measured by dropping 10 µl of solvents or electrolytes on the coated Si wafer. The H-cell experiment was performed in an Ar environment (glove box) at room temperature with both sides of the H-cell under constant stirring (200 r.p.m.). The caps of the H-cell were left loose. One-hundred milligrams of polymer was sandwiched between two layers of separators. The experiment was run for 3 h before stopping, and a picture of the liquid level was taken. Afterwards, 1 ml of the liquids from both sides was collected and 100 µl of 1,1,2,2- tetrafluoroethyl-2,2,3,3-tetrafluoropropyl ether (TTE) was added into the solution as internal concentration standard. F-NMR experiments were performed on a Varian 400 MHz NMR, and the concentration of Li salt was calculated. The ^1H NMR and ^{13}C NMR spectra (500 MHz) were recorded on a Bruker DRX 500 NMR spectrometer in deuterated solvents at 25 °C. The chemical

shift data for each signal are reported in units of δ (p.p.m.). The rheological measurements were conducted on a TA ARES G2 rheometer with an 8 mm parallel plate geometry. The ionic conductivity was measured with a biologic VMP3 system at room temperature in SS||SS (stainless steel) coin cell geometry. The XPS profile was collected on a PHI VersaProbe 3 XPS with an Al K-alpha source, and the sample was transferred from the Ar glove box to the testing stage in an airtight vessel. The O1s XPS was collected after the sample surface was sputtered with Ar at 2 kV 1 µA for 2 min.

Electrochemical characterization

Li||Cu cells were assembled with thick Li chip (1 cm^2) and polymer-coated Cu electrodes with 40 µl of electrolyte and the Celgard 2325 separator. For CE measurements, the electrode surface was first cleaned by ten cycles of charge and discharge at 0.02 mA cm^{-2} between 0 V and 1 V. Then, 5 mAh cm^{-2} was deposited at 0.5 mA cm^{-2}, followed by ten cycles of strip and plate at the same current density and 1 mAh cm^{-2} capacity, and finally completely stripping the deposited lithium from the copper electrode. The XPS signal was collected on the Cu electrode cycled at 0.5 mA cm^{-2} current density and 1 mAh cm^{-2} capacity for ten cycles. For the SEM images, we plated and stripped 1 mAh cm^{-2} of Li at the current density of 0.5 mA cm^{-2} for five cycles before plating 1 mAh cm^{-2} of Li at the same current density. Before the SEM imaging, the sample was quickly dipped in 1,3-trifluorobenzene to remove the polymer coating and excess salt and solvent molecules. Li electrode was dip coated with 0.1 g ml^{-1} SP^2 polymer suspended in anhydrous THF solvent. The electrode was dried in the Ar environment at 80 °C for 8 h before being assembled into a coin cell. All cells were rested for 8 h before cycling.

Data availability

The datasets analysed and generated during the current study are included in the paper and its Supplementary Information file. Source data are provided with this paper.

References

1. Whittingham, M. History, evolution, and future status of energy storage. *Proc. IEEE* **100**, 1518–1534 (2012).
2. Tikekar, M. D., Choudhury, S., Tu, Z. & Archer, L. A. Design principles for electrolytes and interfaces for stable lithium-metal batteries. *Nat. Energy* **1**, 16114 (2016).
3. Cheng, X.-B., Zhang, R., Zhao, C.-Z. & Zhang, Q. Toward safe lithium metal anode in rechargeable batteries: a review. *Chem. Rev.* **117**, 10403–10473 (2017).
4. Lin, D., Liu, Y. & Cui, Y. Reviving the lithium metal anode for high-energy batteries. *Nat. Nanotechnol.* **12**, 194–206 (2017).
5. Liu, S. et al. Salt-in-salt reinforced carbonate electrolyte for Li metal batteries. *Angew. Chem. Int. Ed. Engl.* **61**, e202210522 (2022).
6. Song, J., Si, Y., Guo, W., Wang, D. & Fu, Y. Organosulfide-based deep eutectic electrolyte for lithium batteries. *Angew. Chem. Int. Ed. Engl.* **60**, 9881–9885 (2021).
7. Xue, W. et al. Ultra-high-voltage Ni-rich layered cathodes in practical Li metal batteries enabled by a sulfonamide-based electrolyte. *Nat. Energy* **6**, 495–505 (2021).
8. Zhao, Y. et al. Fluorinated ether electrolyte with controlled solvation structure for high voltage lithium metal batteries. *Nat. Commun.* **13**, 2575 (2022).
9. Holoubek, J. et al. Tailoring electrolyte solvation for Li metal batteries cycled at ultra-low temperature. *Nat. Energy* **6**, 303–313 (2021).
10. Yang, Y. et al. Liquefied gas electrolytes for wide-temperature lithium metal batteries. *Energy Environ. Sci.* **13**, 2209–2219 (2020).
11. Jin, Y. et al. Low-solvation electrolytes for high-voltage sodium-ion batteries. *Nat. Energy* **7**, 718–725 (2022).
12. Zhao, Y. et al. Natural SEI-inspired dual-protective layers via atomic/molecular layer deposition for long-life metallic lithium anode. *Matter* **1**, 1215–1231 (2019).
13. Gao, Y. et al. Low-temperature and high-rate-charging lithium metal batteries enabled by an electrochemically active monolayer-regulated interface. *Nat. Energy* **5**, 534–542 (2020).
14. Gao, Y. et al. Polymer–inorganic solid–electrolyte interphase for stable lithium metal batteries under lean electrolyte conditions. *Nat. Mater.* **18**, 384–389 (2019).
15. Lopez, J., Mackanic, D. G., Cui, Y. & Bao, Z. Designing polymers for advanced battery chemistries. *Nat. Rev. Mater.* **4**, 312–330 (2019).
16. Zhou, H., Yu, S., Liu, H. & Liu, P. Protective coatings for lithium metal anodes: recent progress and future perspectives. *J. Power Sources* **450**, 227632 (2020).
17. Liu, K. et al. Lithium metal anodes with an adaptive 'solid–liquid' interfacial protective layer. *J. Am. Chem. Soc.* **139**, 4815–4820 (2017).
18. Zheng, G. et al. High-performance lithium metal negative electrode with a soft and flowable polymer coating. *ACS Energy Lett.* **1**, 1247–1255 (2016).
19. Kong, X., Rudnicki, P. E., Choudhury, S., Bao, Z. & Qin, J. Dendrite suppression by a polymer coating: a coarse-grained molecular study. *Adv. Funct. Mater.* **30**, 1910138 (2020).
20. Huang, Z. et al. Effects of polymer coating mechanics at solid-electrolyte interphase for stabilizing lithium metal anodes. *Adv. Energy Mater.* **12**, 2103187 (2022).
21. Yu, Z. et al. A dynamic, electrolyte-blocking, and single-ion-conductive network for stable lithium-metal anodes. *Joule* **3**, 2761–2776 (2019).
22. Tu, Z. et al. Designing artificial solid-electrolyte interphases for single-ion and high-efficiency transport in batteries. *Joule* **1**, 394–406 (2017).
23. Baran, M. J. et al. Diversity-oriented synthesis of polymer membranes with ion solvation cages. *Nature* **592**, 225–231 (2021).
24. Stalin, S. et al. Ultrathin zwitterionic polymeric interphases for stable lithium metal anodes. *Matter* **4**, 3753–3773 (2021).
25. Kim, J.-M. et al. High current-density-charging lithium metal batteries enabled by double-layer protected lithium metal anode. *Adv. Funct. Mater.* **32**, 2207172 (2022).
26. Zhou, H. et al. Quantification of the ion transport mechanism in protective polymer coatings on lithium metal anodes. *Chem. Sci.* **12**, 7023–7032 (2021).
27. Lang, J. et al. One-pot solution coating of high-quality LiF layer to stabilize Li metal anode. *Energy Storage Mater.* **16**, 85–90 (2019).
28. Liu, Y. et al. Solubility-mediated sustained release enabling nitrate additive in carbonate electrolytes for stable lithium metal anode. *Nat. Commun.* **9**, 3656 (2018).
29. Liu, H.-J. et al. Engineering lithiophilic silver sponge integrated with ion-conductive PVDF/LiF protective layer for dendrite-free and high-performance lithium metal batteries. *ACS Appl. Energy Mater.* **6**, 519–529 (2023).
30. Guo, Q. et al. CNT/PVDF composite coating layer on Cu with a synergy of uniform current distribution and stress releasing for improving reversible Li plating/stripping. *ACS Appl. Mater. Interfaces* **14**, 46043–46055 (2022).
31. Li, T. et al. Stable anion-derived solid electrolyte interphase in lithium metal batteries. *Angew. Chem. Int. Ed. Engl.* **60**, 22683–22687 (2021).
32. Ren, X. et al. Enabling high-voltage lithium-metal batteries under practical conditions. *Joule* **3**, 1662–1676 (2019).
33. Yu, Z. et al. Rational solvent molecule tuning for high-performance lithium metal battery electrolytes. *Nat. Energy* **7**, 94–106 (2022).
34. Ren, X. et al. Localized high-concentration sulfone electrolytes for high-efficiency lithium-metal batteries. *Chem* **4**, 1877–1892 (2018).

35. Sun, J., O'Dell, L. A., Armand, M., Howlett, P. C. & Forsyth, M. Anion-derived solid-electrolyte interphase enables long life Na-ion batteries using superconcentrated ionic liquid electrolytes. *ACS Energy Lett.* **6**, 2481–2490 (2021).
36. Lopez, J. et al. Effects of polymer coatings on electrodeposited lithium metal. *J. Am. Chem. Soc.* **140**, 11735–11744 (2018).
37. Volkov, A. *Encyclopedia of Membranes* (eds Drioli, E. & Giorno, L) 1–2 (Springer, 2013).
38. Marciniec, B. *Hydrosilylation: A Comprehensive Review on Recent Advances* (Springer, 2008).
39. Pang, Q. et al. Tuning the electrolyte network structure to invoke quasi-solid state sulfur conversion and suppress lithium dendrite formation in Li–S batteries. *Nat. Energy* **3**, 783–791 (2018).
40. Wang, X. et al. Poly(ionic liquid)s-in-salt electrolytes with co-coordination-assisted lithium-ion transport for safe batteries. *Joule* **3**, 2687–2702 (2019).
41. Wong, D. H. C. et al. Nonflammable perfluoropolyether-based electrolytes for lithium batteries. *Proc. Natl Acad. Sci. USA* **111**, 3327–3331 (2014).
42. Huang, Z., Choudhury, S., Gong, H., Cui, Y. & Bao, Z. A cation-tethered flowable polymeric interface for enabling stable deposition of metallic lithium. *J. Am. Chem. Soc.* **142**, 21393–21403 (2020).
43. Henderson, W. A. & Passerini, S. Phase behavior of ionic liquid–Lix mixtures: pyrrolidinium cations and TFSI-anions. *Chem. Mater.* **16**, 2881–2885 (2004).
44. Yu, Z. et al. Molecular design for electrolyte solvents enabling energy-dense and long-cycling lithium metal batteries. *Nat. Energy* **5**, 526–533 (2020).
45. Etacheri, V. et al. Effect of fluoroethylene carbonate (FEC) on the performance and surface chemistry of Si-nanowire Li-ion battery anodes. *Langmuir* **28**, 965–976 (2012).
46. Xiao, J. et al. Understanding and applying coulombic efficiency in lithium metal batteries. *Nat. Energy* **5**, 561–568 (2020).
47. Cao, X., Jia, H., Xu, W. & Zhang, J.-G. Review—localized high-concentration electrolytes for lithium batteries. *J. Electrochem. Soc.* **168**, 010522 (2021).
48. Bieker, G., Winter, M. & Bieker, P. Electrochemical in situ investigations of SEI and dendrite formation on the lithium metal anode. *Phys. Chem. Chem. Phys.* **17**, 8670–8679 (2015).
49. Zhang, W. et al. Engineering wavy-nanostructured anode interphases with fast ion transfer kinetics: toward practical Li-metal full batteries. *Adv. Funct. Mater.* **30**, 2003800 (2020).
50. Li, S. et al. Synergistic dual-additive electrolyte enables practical lithium-metal batteries. *Angew. Chem. Int. Ed. Engl.* **59**, 14935–14941 (2020).
51. Wang, D. et al. Phase-separation-induced porous lithiophilic polymer coating for high-efficiency lithium metal batteries. *Nano Lett.* **21**, 4757–4764 (2021).
52. Zhang, K. et al. A high-performance lithium metal battery with ion-selective nanofluidic transport in a conjugated microporous polymer protective layer. *Adv. Mater.* **33**, 2006323 (2021).
53. Cao, X. et al. Monolithic solid–electrolyte interphases formed in fluorinated orthoformate-based electrolytes minimize Li depletion and pulverization. *Nat. Energy* **4**, 796–805 (2019).
54. Cao, X. et al. Optimization of fluorinated orthoformate based electrolytes for practical high-voltage lithium metal batteries. *Energy Storage Mater.* **34**, 76–84 (2021).
55. Xue, W. et al. FSI-inspired solvent and 'full fluorosulfonyl' electrolyte for 4 V class lithium-metal batteries. *Energy Environ. Sci.* **13**, 212–220 (2020).
56. Huang, Z. et al. A solvent-anchored non-flammable electrolyte. *Matter* **6**, 445–459 (2023).

Acknowledgements

We acknowledge support from the Assistant Secretary for Energy Efficiency and Renewable Energy, Office of Vehicle Technologies of the US Department of Energy under the Battery Materials Research (BMR) Program and the Battery 500 Consortium. Part of this work was performed at the Stanford Nano Shared Facilities (SNSF), supported by the National Science Foundation under award ECCS-1542152. Z.H. acknowledges support from the American Association of University Women international fellowship.

Author contributions

Z.H., Y. Cui and Z.B. conceived the idea. J.-C.L. designed and synthesized related polymers. Z.H. designed and conducted material characterizations and electrochemical measurements. S.-L.L. performed the DFT calculations. Z.Y. helped with the materials characterization and provided the FDMB electrolyte. H.G. and W.Y. conducted the XPS characterization. Y. Chen performed the NMR. X.G. contributed to the H-cell experiment design. J.Q. contributed to the data discussion. All authors discussed and analysed the data. Z.H., J.-C.L., Y. Cui and Z.B. wrote and revised the paper.

Competing interests

For Z.H., J.-C.L., Y. Cui and Z.B., this work has been filed as a US Provisional Patent Application, patent number 63/402,427. The other authors declare no competing interest.

Additional information

Supplementary information The online version contains supplementary material available at https://doi.org/10.1038/s41560-023-01252-5.

Correspondence and requests for materials should be addressed to Yi Cui or Zhenan Bao.

Peer review information *Nature Energy* thanks George Chen, Min-Sik Park and the other, anonymous, reviewer(s) for their contribution to the peer review of this work.